Environmental Science Nano

ROYAL SOCIETY OF CHEMISTRY

PAPER

View Article Online
View Journal | View Issue

Cite this: *Environ. Sci.: Nano*, 2026, **13**, 268

Engineering plastic nanoparticles for super-resolution tracking of lipid membrane interactions

Edin Osmanbasic, † Diyali Sil, † Gauri Tripathi, Jahid Haider, Anaranya Ghorai and Chayan Dutta *

Single-particle measurements are essential for understanding the complex and often subtle interactions of engineered nanoparticles with biological systems. However, the preparation of plastic nanoparticles (PNP) for single-particle experiments has been hindered by challenges in reproducibility and fluorescence functionality. Here, we use a robust and simple method for preparing fluorescently labeled PNPs using a confined impingement jet with dilution (CIJ-D) mixer. We prepared PNPs from polystyrene (PS), polypropylene (PP), polyvinyl chloride (PVC), and polylactic acid (PLA) powders with a narrow particle size distribution (between 50–100 nm) and incorporated Nile red (NR) dye into these particles. These PNPs exhibit colloidal stability, uniform fluorescence intensity, and compatibility with single particle tracking measurements. To demonstrate the applicability of our approach, we tracked the interactions of individual PNP with lipid bilayer surfaces composed of 1-palmitoyl-2-oleoyl-*sn*-glycero-3-phosphocholine (POPC) and cholesterol. Using super-resolution diffusion analysis (fluorescence correlation spectroscopy super-resolution optical fluctuation; fcsSOFI), we characterized the nanoscale diffusion and interaction dynamics of PNPs on the lipid bilayer surface. While electrostatic interactions play a major role in PNP transport dynamics on the bilayer, cholesterol induces slower surface diffusion. Our method provides an easy solution to prepare model PNP systems and study the PNP-membrane interactions using single-particle fluorescence microscopy.

Received 2nd July 2025,
Accepted 15th November 2025

DOI: 10.1039/d5en00599j

rsc.li/es-nano

Environmental significance

Plastic nanoparticles (PNPs) or nanoplastics are ubiquitous and cause significant environmental and health risks. Understanding how PNP interacts with lipid membranes is crucial for insights into membrane-related processes. Due to the lack of reliable PNP model systems, researchers often use commercial polymer beads. Here, we present a simple method to prepare fluorescent PNPs tailored for single particle tracking and nanoscale diffusion analysis on lipid membranes. We show that electrostatic interactions, polarity of PNP particles, and membrane composition critically influence PNP diffusion behavior on membrane surfaces. Our approach provides a robust method for fabricating PNPs optimized for single-particle fluorescence studies, advancing research on the environmental impact of nanoplastics.

Introduction

Plastic pollution is a critical environmental issue of the 21st century, with plastics accumulating in various ecosystems and impacting both wildlife and human health.[1–3] As plastics degrade, they fragment into nanoscale plastic nanoparticles (PNPs) typically less than 1 μm in size,[4] which pose unique threats to biological systems due to their small size, large surface area, and stable chemical properties.[5] While much research has been focused on microplastics (particles with sizes between 1 μm and 5 mm), the behavior, interactions, and toxicity of PNPs remain underexplored.[5] One of the primary reasons for the lack of PNP research is the lack of effective single-particle models. Bulk studies provide limited insight into the dynamics of PNPs, as they fail to account for the heterogeneity inherent in particle interactions at the single-particle level.[6] Furthermore, the non-fluorescent nature of PNPs makes it difficult to track and characterize their interactions in complex biological systems using optical microscopy.

Fluorescence imaging is a powerful tool for visualizing and tracking nanoparticles *in situ*.[7] Fluorescent PNPs allow the tracking of individual particles,[8] enabling the investigation of their interactions with biological surfaces. Single-particle tracking (SPT) techniques[9–12] offer unique insights into the diffusion, aggregation, and interaction of PNPs in complex systems, such as lipid bilayers, cell membranes, and other biological structures. By providing high temporal and spatial resolution, single-particle methods

Georgia State University, Atlanta, 30303, USA. E-mail: cdutta@gsu.edu
† These authors contributed equally.

allow for a detailed understanding of the dynamics of PNPs that can be complementary to traditional bulk measurements.[13]

One of the main obstacles in using fluorescent PNPs for single-particle experiments is the fabrication of well-characterized, reproducible, and environmentally relevant PNPs.[14–17] Commercial polymer beads tagged with fluorescent dyes are often used as model systems in particle tracking studies.[18,19] However, the problem with commercially available fluorescent polymer beads is that their properties are often not fully disclosed. Specifically, the type, quantity, and stability of the dye attached to each bead are commonly unknown. This lack of transparency makes it difficult to quantify and interpret results from single-particle experiments. Moreover, commercial particles may not accurately mimic the size, surface characteristics, or chemical composition of environmental PNPs, limiting their utility. Also, the available PNP type is limited mainly to polystyrene (PS) plastics, limiting most studies to only PS particles.

Accurate characterization of fluorescent PNPs is critical for reliable single-particle experiments. The size of PNPs plays a key role in biological interactions, with smaller particles more likely to penetrate membranes and larger ones prone to aggregation.[20–22] It is also important to quantify the number of fluorescent dye molecules per particle, as dye loading affects fluorescence intensity, stability, and data interpretation.[23] Addressing these challenges with well-defined size distributions and consistent dye quantification is essential for advancing PNP interaction studies.

Here, we present a novel approach to preparing fluorescent PNPs that address these challenges. We used a confined impingement jet with dilution (CIJ-D) mixer method to prepare fluorescent PNPs with narrow size distribution and fluorescent dye loading. We customized the CIJ-D technique to incorporate Nile red (NR), a commonly used hydrophobic dye. NR is widely employed in fluorescence studies due to its stability and strong emission, making it an ideal choice for labeling hydrophobic nanoparticles.[23,24] To quantify the dye loading in the synthesized nanoparticles, we employed a combination of absorption calibration and Mie scattering analysis.[25] We also used dynamic light scattering (DLS) and particle tracking to assess the size of the particles. SPT measurements allowed us to directly observe the behavior of individual PNP in real-time, providing valuable insights into their interactions with lipid bilayer surfaces.

To explore the utility of fluorescent PNPs, we conducted proof-of-concept experiments tracking individual PNPs on lipid bilayers composed of 1-palmitoyl-2-oleoyl-*sn-glycero*-3-phosphocholine (POPC) and cholesterol, which serve as widely used model systems for studying cellular membranes. Cholesterol,[26] a major component of cell membranes, introduces rigidity to the bilayer, which can affect the diffusion and interaction dynamics of nanoparticles. We performed diffusion analysis on the fluorescent PNP-membrane interactions using super-resolution fluorescence correlation spectroscopy super-resolution optical fluctuation imaging (fcsSOFI). Our findings revealed differences in the diffusion properties of the PNPs on POPC *versus* POPC-cholesterol bilayers, providing insight into the impact of membrane rigidity on nanoparticle behavior. Specifically, we observed that the PNPs diffused more freely on the POPC bilayer, while their movement was restricted on the cholesterol-containing membrane. These results underscore the importance of membrane composition in modulating the behavior of PNPs and suggest that the rigidification of the membrane surface may influence nanoparticle uptake and interaction dynamics.

We used engineered PNPs to explore the heterogeneity of their behavior at the single-particle level, which provided valuable insight into their interactions with lipid bilayers. Our results highlight the importance of using engineered PNPs over commercial beads, particularly in terms of their relevance to biological studies. The ability to control particle characteristics, such as size, fluorescence, and surface properties, opens new opportunities for studying the transport, accumulation, and potential toxicity of PNPs in complex biological systems. Ultimately, this study contributes to the growing body of research aimed at developing accurate, reproducible, and environmentally relevant models for studying PNPs, providing a crucial tool for advancing our understanding of these ubiquitous particles.

Materials and methods

Designing the CIJ-D mixer

The custom-built CIJ-D mixer assembly is shown in Fig. 1. The CIJ-D mixer was manufactured in the machine shop and is made of Teflon. The mixer works using a technique called 'flash nanoprecipitation',[27] where polymer dissolved in an organic solvent is rapidly mixed with an antisolvent of much lower solubility. This rapid mixing causes supersaturation of the polymer, leading to precipitation into nanoparticles.[28] The size of the nanoparticles is controlled by the flow rate and the solvent/antisolvent ratio.[29,30] A large turbulent flow of the solvent and anti-solvent was achieved inside a small chamber, pumped into the mixer using two low-friction microliter glass syringes. Mixing takes place inside the small chamber from two inputs, one containing plastic polymers dissolved in organic solvent, and the other consisting of antisolvent (Millipore H_2O), as illustrated in Fig. 1A.

The computer-aided design of the assembly is illustrated in Fig. 1B. The assembly was divided into two parts (Fig. S1A and S1B) and was assembled using rubber O-rings and screws. The critical dimensions associated with the mixer are outlined in Fig. S1C. The ratio of the chamber height above the inlet nozzle to the diameter was kept at 0.5 while the outlet length to outlet diameter ratio was maintained at greater than 10. This factor is kept greater than 10 to ensure a drop in pressure so that the chamber remains

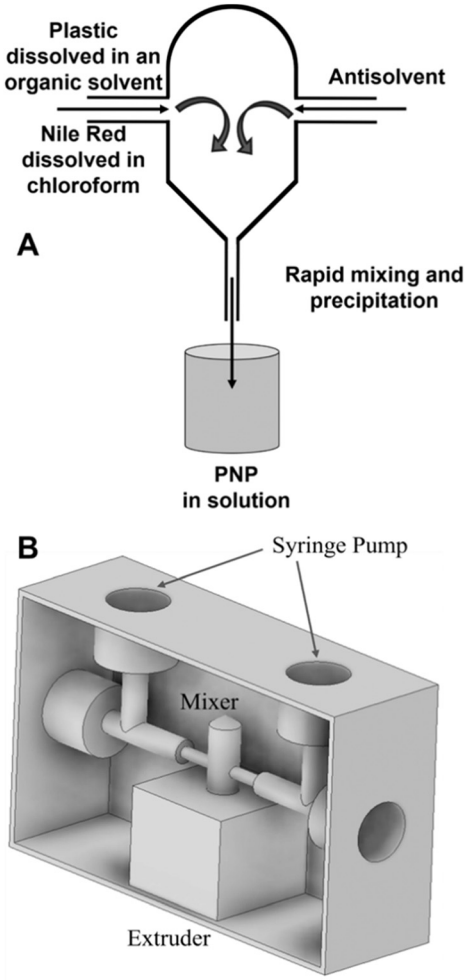

Fig. 1 Flash nanoprecipitation for preparing fluorescent PNPs. (A) Schematic of the rapid mixing process, where a mixture of plastics (dissolved in an organic solvent) and NR dye (dissolved in chloroform) is introduced in the CIJ-D mixer along with an antisolvent, leading to the instantaneous precipitation of fluorescent PNPs. (B) CAD rendering of custom-built CIJ-D mixer.

filled during impingement. The microliter glass syringes were obtained from Hamilton and were connected to the assembly *via* threaded adapters. The side openings in the assembly were required due to machining constraints and were sealed using M6 plugs during the nano-precipitation process.

Source of plastics for PNP preparation

We obtained plastics powders from a company (Keyeu Materials) that sells plastics in powder form for use in different industrial applications. These plastic powders are used in our everyday products; thus, PNPs made from these sources are representative of PNPs we might often encounter in our environment. We used polypropylene (PP), polystyrene (PS), polyvinyl chloride (PVC), and polylactic acid (PLA) for our current study and prepared PNPs using the CIJ-D mixture.

Preparation of PNPs using the CIJ-D mixer

PNPs were synthesized using a custom-designed CIJ-D mixer developed in our lab, with modifications to maintain an outlet length-to-diameter ratio of 15.[27] The plastic powders were dissolved in an organic solvent, along with 750 μg of NR dye dissolved completely in chloroform.[23] The solution was then heated to 50 °C and stirred at 300 rpm for an hour. 0.5 mL of the plastic solution was injected into one side of the CIJ-D mixer, and 0.5 mL of the antisolvent (Millipore H_2O) was injected through the opposite side at the same injection rate. For PS, PVC, and PLA, the solvent and antisolvent were DMF and Millipore H_2O, respectively, whereas for PP the solvent was toluene and the antisolvent was DMF.

The injection rate was estimated to be ~12 mL min^{-1}, as injection was done by hand with Hamilton Co. GasTight #1001 glass syringes. The injection rate affects the resulting particle size, where faster injection rates lead to smaller particles.[27] Injection rates are expressed as Reynold's numbers (Re), which is calculated by eqn (1).

$$\mathrm{Re} = \frac{4}{\pi d}\sum_{i=1}^{n}\frac{\rho_i Q_i}{\mu_i} \quad (1)$$

where d is the inlet diameter, n is the total number of inlet streams, ρ_i is the density of the fluid of the ith stream, Q_i is the volumetric flow rate for the ith stream, and μ_i is the viscosity of the fluid for the ith stream. Our inlet diameters were 1×10^{-3} m, with $n = 2$ streams, the density of water and DMF at room temperature being 1.00×10^3 kg m^{-3} and 9.48×10^2 kg m^{-3} respectively, the viscosity of water and DMF at room temperature being 8.90×10^{-4} Pa s and 8.02×10^{-4} Pa s respectively, and the volumetric flow rate of each stream being 2.00×10^{-7} m^3 s^{-1}, we calculated Re ≈ 590. For a more controlled synthesis of particles with smaller and larger size distribution (as shown in the SI), we used a two-channel syringe pump (New Era Pump Systems, Inc.) that provided more control over the injection rate and the Reynold's number.

The resulting suspension poured out of the outlet port of the CIJ-D mixer into a beaker containing 9 mL of antisolvent. 1 mL of the resulting suspension was then filtered through a 0.22 micron mixed cellulose esters (MCE) membrane filter, centrifuged, and had supernatant removed and replaced with an equal amount of antisolvent. This process was repeated three times to remove the organic solvent and the free dye from the solution. For PS, PVC, and PLA, the solvent and antisolvent were DMF and millipore H_2O, respectively, whereas for PP solvent was toluene and antisolvent was DMF. Here, we have selected only these polymers to make model PNPs, however, it is possible to make any type of PNPs using this method if the plastic polymer can be dissolved in an organic solvent.

Scanning electron microscope (SEM) measurement

PNP samples without fluorescent dyes were deposited on cleaned silicon wafers and mounted to standard aluminum

stubs. The samples were then coated with an approximately 15 nm layer of gold by using a Denton Vacuum Desk II sputter coater (Moorestown, NJ). Imaging was performed using a TESCAN VEGA 3 scanning electron microscope (Brno, Czech Republic) equipped with a tungsten electron source. The samples were imaged at 10 kV accelerating voltage using a secondary electron detector.

Dynamic light scattering (DLS) measurements for particle hydrodynamic radii

A DynaPro Nanostar II Dynamic Light Scattering Instrument (2nd generation) from Wyatt Technology was used for measuring the size of PNPs. An incident wavelength of 663.1 nm was used with 100.0% laser power at 25 °C (room temperature) to perform the DLS measurement. This instrument can measure particle size ranging from 0.2 nm to 1000 nm. The DLS detector angle was set to 90°, and the solvent used was Millipore H_2O. The refractive index of the solvent was 1.333, and the solvent viscosity (cP) was 0.89. The PNP suspensions were sonicated for 15 minutes, then filtered using a 0.22 μm MCE pore size syringe filter to measure particle size *via* DLS. Sonication and filtration were performed to remove any aggregates that formed after prolonged storage of the plastic solutions. A disposable microcuvette (micro/cuvette kit for the Nanostar™ II) from Wyatt Technology was used in the DLS cuvette holder, which can hold a minimum volume of 4 mL.

Absorption and emission measurements

Absorption spectra of NR, NR-tagged, and untagged PNPs were collected in a PerkinElmer Lambda 35 spectrophotometer. Emission spectra were recorded in a PerkinElmer LS 55 spectrofluorometer. Both absorption and emission data were analyzed and plotted using MATLAB.

Quantifying the number of dye molecules in single PNPs

We quantified the number of PNPs in the suspension and the number of molecules of NR in each PNP particle with measurements in absorption spectroscopy. An absorbance and emission calibration curve based on decreasing concentrations of NR (Fig. S2) was collected to locate the absorption and emission maxima (λ_{max}) of NR. The molar absorption coefficient (ε) of NR was calculated from the Beer–Lambert law, $A = \varepsilon lc$. The absorption spectra of NR-tagged PNPs were collected, and the λ_{max} of each spectrum was defined. The absorption spectra of NR-tagged PNPs were used to calculate the number of NR molecules in each PNP, while the absorption spectra of untagged PNPs were collected to calculate the number of particles in the suspension of PNPs. In eqn (2), absorbance (α_{ext}) is related to the extinction efficiency of the suspension Q_{ext}, the radius of the particles r, the path length of the cell l, and the particle density in the suspension N.[31]

$$N(r,c) = \frac{\alpha_{ext}(\lambda_{max})}{Q_{ext}(r, \lambda_{max}, m)A(r)l} \quad (2)$$

$$Q_{ext} = \frac{2}{x^2}\sum_{n=1}^{\infty}(2n+1)\mathrm{Re}(a_n + b_n) \quad (3)$$

In eqn (3), x is the diffraction diameter, equal to ka, k is the wave number, equal to $\frac{2\pi n_m}{\lambda_0}$, λ_0 is the vacuum wavelength of the light, set to λ_{max}, a_n and b_n are the real components of the Mie coefficients for a scattered wave, which depend on x and the complex refractive index m, equal to $\frac{(n_p + ik_p)}{(n_m + ik_m)}$, and $(n_p + ik_p)$ and $(n_m + ik_m)$ are the complex refractive indices of the particles and the medium of the suspension, respectively. Rearranging eqn (2), the number density of the PNP suspensions was calculated. The complex refractive indices varied per plastic, and the values used for our calculations are provided in Table S1, along with all calculation steps, are provided in the SI.

Fourier transform infrared (FTIR) spectroscopy measurements

ATR-FTIR spectra of powdered plastics were recorded using a Perkin Elmer Spectrum 100 FTIR spectrometer equipped with a Universal ATR sampling accessory. 4 scans were acquired within a spectral range of 650–4000 cm^{-1}. The spectra were processed and analyzed using Perkin Elmer's Spectrum IR software. All FTIR spectra of the plastic powders are provided in Fig. S3. The FTIR spectra of four plastic powders (Fig. S3) confirms characteristic vibrational features consistent with literature reports. PLA shows a strong C═O stretch at 1750 cm^{-1} and ester C–O stretching at 1181 cm^{-1}. PP exhibits CH_3 and CH_2 stretching and bending modes between 2952–2838 cm^{-1} and 1452–1376 cm^{-1}. PVC displays C–H stretching and bending bands, with an additional absorption at ~1715 cm^{-1} attributed to oxygenated additives. PS is identified by distinct aromatic C–H and C═C stretching bands, verifying its aromatic ring structure. Additional details are noted in the SI.

Total internal reflection fluorescence (TIRF) imaging

Single-particle fluorescence images of engineered PNPs on supported lipid bilayers were obtained using a wide-field TIRF microscope (Nikon) equipped for video-rate imaging. A 561 nm laser was used for excitation, and the light was directed onto the sample using a 100X oil-immersion objective with a numerical aperture of 1.49. Fluorescence emission was collected over a 512 × 512-pixel area on the sample, and at least 10 videos were recorded for each PNP using an EMCCD camera (Andor, iXon 897). The camera was operated by Andor Solis software in frame transfer mode.

Single particle tracking (SPT) analysis

We used a localization-based single-particle tracking algorithm (Troika[32]) to identify, localize, and track individual

PNPs particles across multiple frames. SPT involves three sequential steps: enhancing the signal-to-noise ratio using a pixel-averaging matrix, identifying particles *via* local intensity maxima and radial symmetry fitting, and linking particle positions frame-to-frame with a nearest-neighbor algorithm to generate trajectories under varying conditions. Troika employs a dynamic nearest-neighbor search radius and global optimization to ensure continuous particle tracking and to minimize misidentification of repeated adsorption events. For trajectory linking, we allowed a single frame gap to be skipped without generating a new trajectory. In cases where one frame was missing, the x and y coordinates were interpolated by taking the midpoint between the preceding and following frames, minimizing trajectory fragmentation caused by transient signal loss. If a particle disappears for more than one frame, a new trajectory is initiated. This approach reduces errors from photoblinking, out-of-focus motion, or particle density fluctuations and ensures trajectories represent continuous motion of individual particles rather than repeated adsorption events. We used a 0.03 second exposure time and 512 × 512-pixel area for SPT analysis. To minimize redundancy and bias, a custom MATLAB script was applied to filter out stuck particles identified in the first frame, a step, particularly necessary under certain conditions (such as in the presence of salt) where immobilized particles were observed from the first frame. We also filtered out trajectories that lasted for 3 frames or less, to reduce non-specific detections. Statistical analysis was performed on the single particle trajectories to evaluate particle behavior across experimental conditions.

Mean square displacement (MSD) and particle size determination

Assuming that all particles are spherical and particles undergo Brownian diffusion in solution, the radius of the particles can be related to their diffusion, using the Stokes–Einstein–Sutherland relation. The details of the process of calculating the hydrodynamic radius for PS are described in Fig. S4. The PNPs were flowed into a microfluidic chamber containing a plasma-cleaned glass coverslip without any lipid bilayer. Microscopy measurements were performed in widefield epi-illumination, where the incident laser illuminates the bulk of the solution[33] such that we can measure the free diffusion of the particles without any interaction from the glass surface (Fig. S4A).[34] An EM gain of 300 was used while recording the data. SPT was performed to approximate the single-molecule trajectories of the PNPs. By using the time-dependent trajectories, MSD ($\langle r^2(\tau)\rangle$) was determined as a function of the time lag (τ) (Fig. S4B), and the average diffusion coefficient D, as seen in eqn (4) (Fig. S4C).

$$\langle r^2(\tau)\rangle = 4D\tau \tag{4}$$

The hydrodynamic radii (R_h) of individual PS-PNPs were calculated using the Stokes–Einstein–Sutherland relation, given as eqn (5) (Fig. S4D).

$$D = \frac{k_b T}{6\pi\eta R_h} \tag{5}$$

where k_b is the Boltzmann constant, T is the absolute temperature of the suspension, and η is the dynamic viscosity of the suspension (water media).

Chemicals for lipid bilayer preparation

POPC and cholesterol from Avanti Polar Lipids, HEPES buffer (pH 7.3) from Quality Biological, chloroform (HPLC grade, stabilized) from VWR Chemicals, and sodium chloride (NaCl, 99% purity) from Beantown Chemical were purchased and used as received. The HEPES buffer, initially at 1 M concentration, was diluted to 20 mM using Millipore water (Avidity Science). To prepare small unilamellar vesicles (SUVs), POPC lipids were first dissolved in chloroform to create a stock solution of 25 mg ml^{-1}, which was subsequently diluted to a working concentration of 5 mg ml^{-1} using the 20 mM HEPES buffer. A cholesterol stock solution of 20 mg ml^{-1} in chloroform was used for the experiments.

Supported lipid bilayer (SLB) preparation

SLB was prepared using the vesicle fusion process.[19,35] POPC lipid, dissolved in HEPES buffer at a concentration of 5 mg ml^{-1}, was extruded through a polycarbonate membrane with 100 nm pores to prepare small unilamellar vesicles (SUVs). Approximately 40 μL of the SUV solution was introduced into a microfluidic chamber, allowing it to interact with the hydrophilic surface of a plasma-cleaned coverslip. After an incubation period of 90 minutes, the chamber was thoroughly rinsed 4 times with HEPES buffer (at least 10 μL each time) to remove excess vesicles. The resulting supported lipid bilayer was then ready for single-particle imaging experiments. For the cholesterol/POPC system, a 3 : 2 ratio of cholesterol to POPC was used during the extrusion process.

Single frame displacement (SFD) analysis

The displacement of PNPs over the membrane surface is quantified using SFD, a measurement that represents the movement of PNPs from one frame to the next. The displacement values are plotted as histograms.

van Hove distribution of displacements

PNP displacement distribution was quantified using the van Hove correlation function (eqn (6)).[36]

$$G_s(\Delta x,\ \Delta t) = \frac{1}{N}\left\langle \sum_{i=1}^{N} \delta(x + x_i(t) - x_i(t + \Delta t)) \right\rangle \quad (6)$$

In eqn (6), δ is the Dirac delta function, x is the current position of the particle along its trajectory, while Δx is the distance the particle travels during time Δt and the angle brackets denote an ensemble average.

fcsSOFI analysis

Super-resolution diffusion maps of lipid bilayer surfaces were generated using the correlation-based fcsSOFI technique to study PNP interactions with cholesterol-rich and cholesterol-free surfaces. fcsSOFI analyzes the stochastic optical fluctuations of independently diffusing emitters on the surface to enhance spatial resolution beyond the diffraction limit, though the enhancement is constrained by the speed of emitter diffusion.[37,38] Diffusion coefficient at each pixel were determined by fitting autocorrelation curves for each pixel using a an anomalous diffusion model as we see non-Gaussian type behavior in the van-Hove distributions.[38] Diffusion values were disregarded if the fit quality was poor ($R^2 < 90\%$). For the fcsSOFI analysis, 1000-frame movies and 128 × 128-pixel region cropped from 512 × 512-pixel area were used to calculate pixel-wise autocorrelations, resulting in an effective temporal resolution of approximately 30 seconds.[37] The data collected for both conditions included spatial and diffusion information, combined into a single super-resolution map. The maps used a color scheme where diffusion values were represented by hue, spatial resolution by saturation, and brightness was kept constant. This approach allowed visualization of PNP interactions on lipid bilayers, highlighting differences between cholesterol-rich and cholesterol-free surfaces.

Results and discussion

We prepared PNPs from plastic polymer powders of PS, PP, PVC, and PLA. Fig. 2 represents the SEM images of our PNPs. We determined the sizes of the PNPs by using the DLS and hydrodynamic radius calculations of freely diffusing particles as discussed previously. Blue circles in Fig. 3 show the size distribution obtained from DLS, with Fig. S5 showcasing the fitting for the autocorrelation *versus* decay time graphs for calculating the sizes of our particles. Our controlled nanoparticle preparation method allowed us to get particles with a narrow distribution. We note here that the average size of the particles mainly depends on the solvent/anti-solvent ratio and on the applied flow rate.[27] We obtained an average particle size of ~35 nm for PP and ~50–80 nm for PS, PVC, and PLA particles. We demonstrated that particle size can be systematically tuned by adjusting the flow rate and the solvent-to-antisolvent ratio. At a fixed Reynolds number of 2800, reducing the solvent/antisolvent ratio from 0.35 to 0.05 decreased the particle size from 300 nm to 90 nm. Likewise, at a constant dilution factor of 0.05, varying the Reynolds number from 2800 to 150 yielded particles of 90 nm and 200 nm, respectively as shown in Fig. S6. The hydrodynamic radius of freely diffusing particles are plotted on the right axis (orange circles) of Fig. 3. All particle sizes measured using SPT measurements showed a narrow distribution (~100–120 nm). Although sample preparation was kept constant across all PNPs, it should be noted that accuracy of the calculated radii of the PNPs vary with each method; SEM represents the actual physical size of the PNPs, while SPT

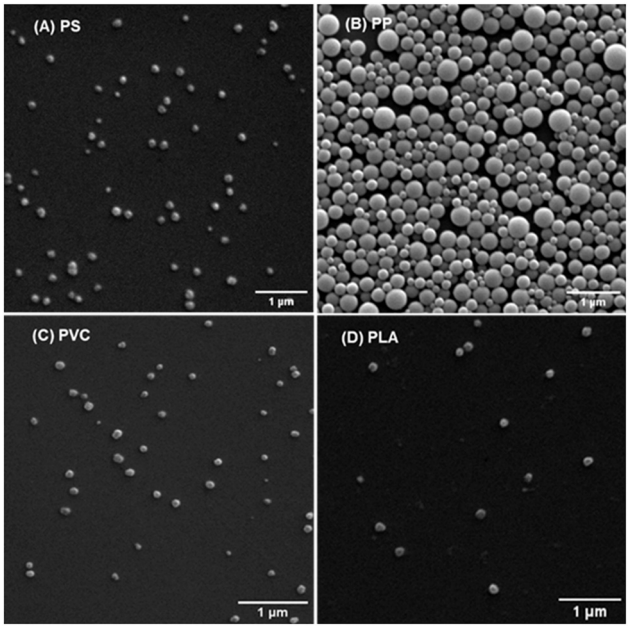

Fig. 2 SEM micrographs of A) PS, B) PP, C) PVC, D) PLA.

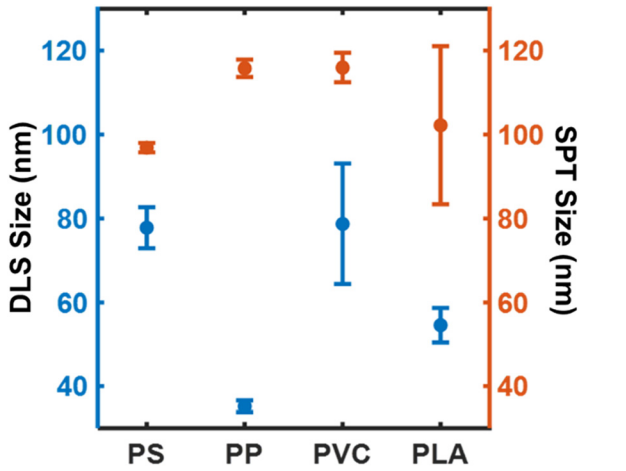

Fig. 3 PNP size estimation using DLS (left axis, blue circles) and SPT (right axis, orange circles). DLS measured sizes represent the average, and the error bars show the standard deviation of at least three independent measurements. SPT sizes are estimated from single particle measurements from approximately 1000 different trajectories, where error bars represent standard deviation across three measurements.

and DLS calculate their hydrodynamic radii. SPT analysis on free diffusing commercial beads provided an average hydrodynamic radius of approximately 57 nm (manufacturer reported average radius is 50 nm), corresponding to a diffusion coefficient of 4.3×10^6 nm2 s^{-1}. Radii calculated using SPT are more reliable than those obtained from DLS in this case, as the latter suffers from a high polydispersity index (PDI) and poor fitting of the scattering plots for our measurements. Additional details are included in the SI.

The fluorescence intensity of the engineered PNPs is lower than the fluorescence intensity of commercially available fluorescent PS beads, as seen in Fig. S7, this is mostly due to different dye used in our experiments and variations in dye loading. We quantified the number of NR dyes in each PNP by measuring the absorption spectra of a solution of NR-tagged PNPs with a known number density of particles (Fig. S8A and S8B). Here we assume that the number density of PNP in the NR untagged solution and the NR-tagged solution are the same, as we use the same protocol for particle preparation and spectra measurement. We estimated the number density of PNPs in each solution using the absorption spectra as detailed in the materials and methods section (and in the SI). We estimate that there are around 0.2 to 8×10^6 NR dyes (Fig. S8C) in each PNPs made with our CIJ-D mixer method. We note here that it is possible to control the number of dyes by changing the initial concentration of the NR dye during the mixing process. Additionally, from the spectral shifts of the emission spectra of NR-tagged PNPs, we found that PVC is the most polar, followed by PLA, PS, and PP, for the commercial plastic samples we used (Fig. S9).

Our measurements reveal two types of particle behavior on the bilayer surface, where some particles undergo free Brownian diffusion while others exhibit confined motion, as

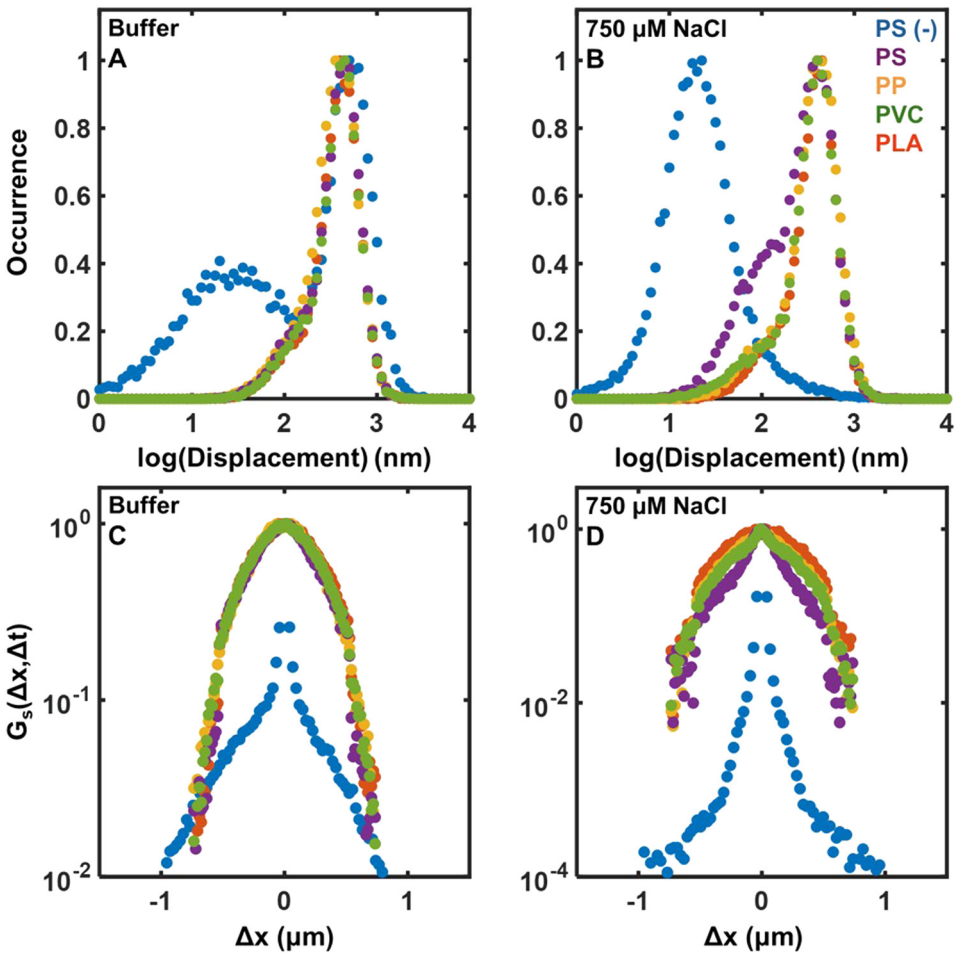

Fig. 4 Single-frame displacement and van Hove distribution demonstrating the diffusion behavior of engineered PNPs on a POPC lipid bilayer surface under buffer and salt conditions. (A) In buffer-only conditions, all PNPs exhibit primarily long displacement distributions, indicative of Brownian-type diffusion, as shown in the population distribution in (C). For comparison, displacement data for commercial carboxy-functionalized polystyrene (PS-) nanoparticles are also shown, which display a bimodal displacement distribution and non-Gaussian behavior. (C) In the presence of 750 μM NaCl, a shoulder appears on the short displacement side of the distribution, suggesting the presence of a second population with shorter displacements. PS(–) particles predominantly show a shorter displacement population. (D) Population distribution reflects a narrow distribution at the center, which shows signs of non-Gaussian confined diffusion. PS(–) in high salt conditions shows the confined diffusion distribution due to surface charge screening and local interaction on the lipid headgroups.

shown in the SI (Fig. S10). To further illustrate these behaviors, we have included two representative videos in the SI. We do not observe hopping dynamics, *i.e.*, repeated association and dissociation from the bilayer surface. Engineered PNP diffusion on the POPC bilayer surface is distinct compared to the commercial PNPs. Fig. 4A shows that all particles show longer displacement with a tailed distribution towards the shorter displacement side. In the presence of 750 μM NaCl, a hump at the shorter displacement side is more prominent showing that higher salt concentrations induce particles to move to shorter distances (Fig. 4B). We calculated that approximately 42% of the engineered PS-PNPs exhibited Brownian diffusion, while 58% displayed confined diffusion under salt conditions. We defined Brownian diffusion as trajectories with anomalous diffusion exponent (α) values between 0.9 and 1.1, accounting for the accuracy of our single-particle tracking approach. Confined diffusion was defined as trajectories with α values below 0.9. Commercial PNPs displacements are plotted for comparison in both conditions (blue curves). We also quantified that 36% of the commercial PS beads showed Brownian diffusion, while 64% experienced confined diffusion. We attribute this larger confined population for the commercial beads to the surface charge of these particles. Similar effects were described previously for PS(−) diffusion on supported POPC bilayers, where increasing NaCl concentration leads to accumulation of Na^+ ions near the negatively charged phosphate groups of POPC. This reduces the shielding of the positively charged amine groups, making them more accessible to PS(−) and thereby enhancing electrostatic interactions that confine particle diffusion.[19] We also observe that the overall width of the distribution for the engineered PNPs is narrower compared to the commercial PS beads. A secondary population with shorter displacements emerged at higher salt concentrations, albeit with lower abundance, suggesting partial confinement and stronger interactions due to ionic screening effects. Notably, PS(−) particles displayed predominantly confined diffusion, likely due to charge screening and specific interactions with lipid headgroups, as shown in our previous study.[19]

Fig. 4C and D show the van Hove distribution for the population in buffer and with high salt conditions, respectively. The van Hove correlation function describes the probability distribution of particle displacements over time. For particles undergoing Brownian motion, the distribution is Gaussian, reflecting random motion with most displacements clustered near zero and fewer large displacements. In contrast, when particles are confined by strong interactions with the bilayer surface, the distribution deviates from Gaussian behavior and develops a sharp central peak with heavier tails, which we describe as non-Gaussian. This deviation indicates restricted diffusion and intermittent trapping, consistent with stronger binding or hindrance at the bilayer. By contrast, particles that interact weakly with the surface exhibit Gaussian displacement statistics characteristic of free diffusion. While we find a Gaussian distribution for all PNPs, the PS(−) shows a non-Gaussian distribution, where short displacements are due to confinement and long displacements are Gaussian type. The population distributions in high-salt conditions (Fig. 4D) further highlighted a transition to non-Gaussian behavior for PS(−) particles, reflecting localized interactions. Notably, non-Gaussian transport can still exhibit a linear mean-squared displacement *versus* time lag (Fig. S11) plot, even though the underlying displacement distribution deviates from a Gaussian form. Particles that interact strongly with the bilayer surface exhibit such non-Gaussian distributions, whereas weakly interacting particles retain the Gaussian profile of free diffusion. For all engineered PNPs, distributions are mixed with confined character at short displacements along with long displacements. While slower Brownian motion within the membrane plane produces a Gaussian displacement distribution, the non-Gaussian behavior observed here arises from intermittent confinement or trapping at the bilayer surface. The resulting displacement distribution can be viewed as a superposition of two components: a narrow Gaussian corresponding to confined or hindered motion and a broader Gaussian or exponential-like tail representing free or Brownian diffusion events. This combination leads to deviations from a single Gaussian profile, which we refer to as non-Gaussian behavior. These results underline the influence of ionic environments on nanoparticle-lipid interactions and the unique diffusive behaviors of engineered PNPs compared to commercial PS beads demonstrating the versatility of these PNPs for lipid bilayer interaction studies.

Cholesterol-rich membrane surfaces are crucial to investigate in the context of PNPs' interactions because cholesterol significantly alters membrane structure and dynamics.[39–41] Cholesterol induces a condensing effect on phospholipid membranes by increasing packing density and reducing fluidity.[42–44] Such changes in membrane properties can affect the adsorption, diffusion, and potential penetration of nanoparticles.[45,46] These changes in physical behavior may amplify or mitigate the disruptive effects of PNPs on cellular membranes, influencing processes such as signaling, permeability, and lipid organization. Cholesterol limits lipid movements and thereby reduces spontaneous uptake of small amphiphilic gold nanoparticles, where nanoparticles' properties also play an important role.[47] Thus, understanding these interactions is essential for assessing the environmental and biological impact of PNPs on cholesterol-rich domains. We performed single-particle tracking experiments on a cholesterol-rich POPC bilayer surface with PLA and PP nanoparticles. The displacement profiles for PLA and PP nanoparticles on the cholesterol-rich POPC/Chol lipid bilayer are similar (Fig. 5A), but they exhibit longer displacements compared to those observed on the POPC bilayer in buffer-only conditions. This suggests that the presence of cholesterol impacts surface diffusion, likely due

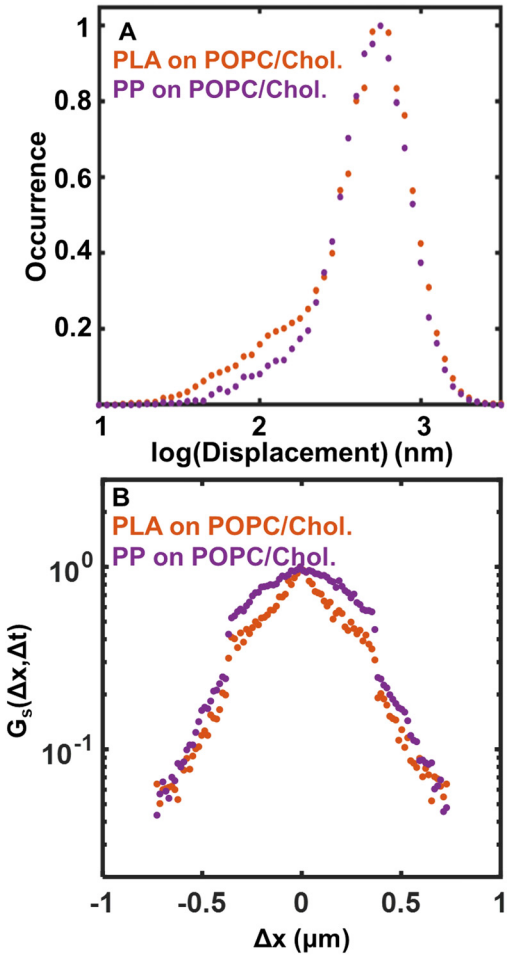

Fig. 5 Single-frame displacement and van Hove distribution of engineered PNPs on POPC lipid bilayer surface and POPC/cholesterol bilayer surface. (A) PLA and PP show one population corresponding to long displacement value for both types of surfaces. (B) PP shows a gaussian distribution indicating Brownian motion whereas PLA exhibits a central peak at the center of the distribution suggesting confined diffusion on the bilayer surface.

to its influence on bilayer packing and interaction dynamics. The surface chemistry induced by cholesterol plays a critical role in modulating nanoparticle mobility and interaction with the lipid membrane. For the van Hove distribution (Fig. 5B), PLA nanoparticles demonstrate the most non-Gaussian behavior, characterized by a prominent narrow distribution at the center. This indicates confined diffusion, potentially arising from stronger local interactions between PLA nanoparticles and specific lipid domains. These observations highlight the importance of both nanoparticle properties and lipid membrane composition in governing surface diffusion and interaction mechanisms.

Spatially resolved fcsSOFI diffusion maps highlight the influence of cholesterol on the diffusion dynamics of PNPs on the lipid bilayer surface. Representative fcsSOFI maps of PP particle diffusion on POPC and POPC/Chl surfaces are shown in Fig. 6A and B, respectively. We observe a more homogeneous distribution on POPC in buffer conditions. Whereas, in the presence of cholesterol, more heterogeneous interactions and lower diffusion coefficients prevail. The cumulative probability distributions of the diffusion coefficients for PLA (Fig. 6C) and PP (Fig. 6D) nanoparticles reveal differences under varying bilayer conditions. While the spatial heterogeneity in POPC *versus* POPC/Chol is very subtle (Fig. 6A and B), the cumulative distributions (Fig. 6C and D) clearly show slower diffusion for both PLA and PP particles in the presence of cholesterol. These results indicate that bilayer composition modulates nanoparticle mobility, with cholesterol reducing diffusion and potentially limiting transport across biological interfaces. PLA nanoparticles exhibit a slight reduction in the mean diffusion coefficient (μ) in the cholesterol-rich POPC/Chol bilayer (μ = 4.98, in log scale) compared to the pure POPC (μ = 5.16) bilayer. The addition of 750 μM NaCl to the POPC bilayer also results in a decrease in the mean diffusion coefficient with respect to buffer (μ = 5.09), indicating the role of salt in reducing mobility, potentially through charge screening effects and stronger particle–lipid interactions. In contrast, PP nanoparticles showed higher diffusion values across the three conditions, with only slight variations in μ and σ. This behavior indicates that nanoparticle chemistry and lipid composition interplay differently for PLA and PP, with PLA showing more pronounced sensitivity to the lipid environment.

The comparison of diffusion constants obtained from SPT and fcsSOFI (Fig. S12) reveals consistent but systematically lower values from fcsSOFI. While single-particle trajectories can provide diffusion constants for the entire particle trajectory, fcsSOFI captures local fluctuations in fluorescence intensity at the pixel level, thereby being more sensitive to nanoscale interactions and confinement effects. The reduced diffusion values observed in fcsSOFI suggest that PP and PLA particles experience heterogeneous local environments and transient interactions. This comparison highlights the complementarity of SPT and fcsSOFI. While SPT offers superior localization precision and robust statistics from thousands of trajectories, fcsSOFI provides spatially resolved maps of diffusion behavior (at each pixel) that reveal heterogeneous interactions and local confinement effects in complex systems, particularly in regimes where SPT performance is limited by trajectory overlap or rapid motion.

In summary, we provide a simple method to engineer fluorescent PNPs optimized for single-particle fluorescence measurements to investigate PNP-membrane interactions. Our results underscore the importance of both lipid bilayer composition and ionic strength in governing the mobility of PNPs on membrane surfaces. Engineered PNP diffusion on POPC bilayer surface follows Brownian type motion but captures more confined diffusion at higher ionic strength contrary to what we have observed before for carboxylated PS(−) bead. Cholesterol alters bilayer packing and fluidity, leading to distinct diffusion behaviors for more polar (PLA) and more non-polar (PP) particles, as revealed through

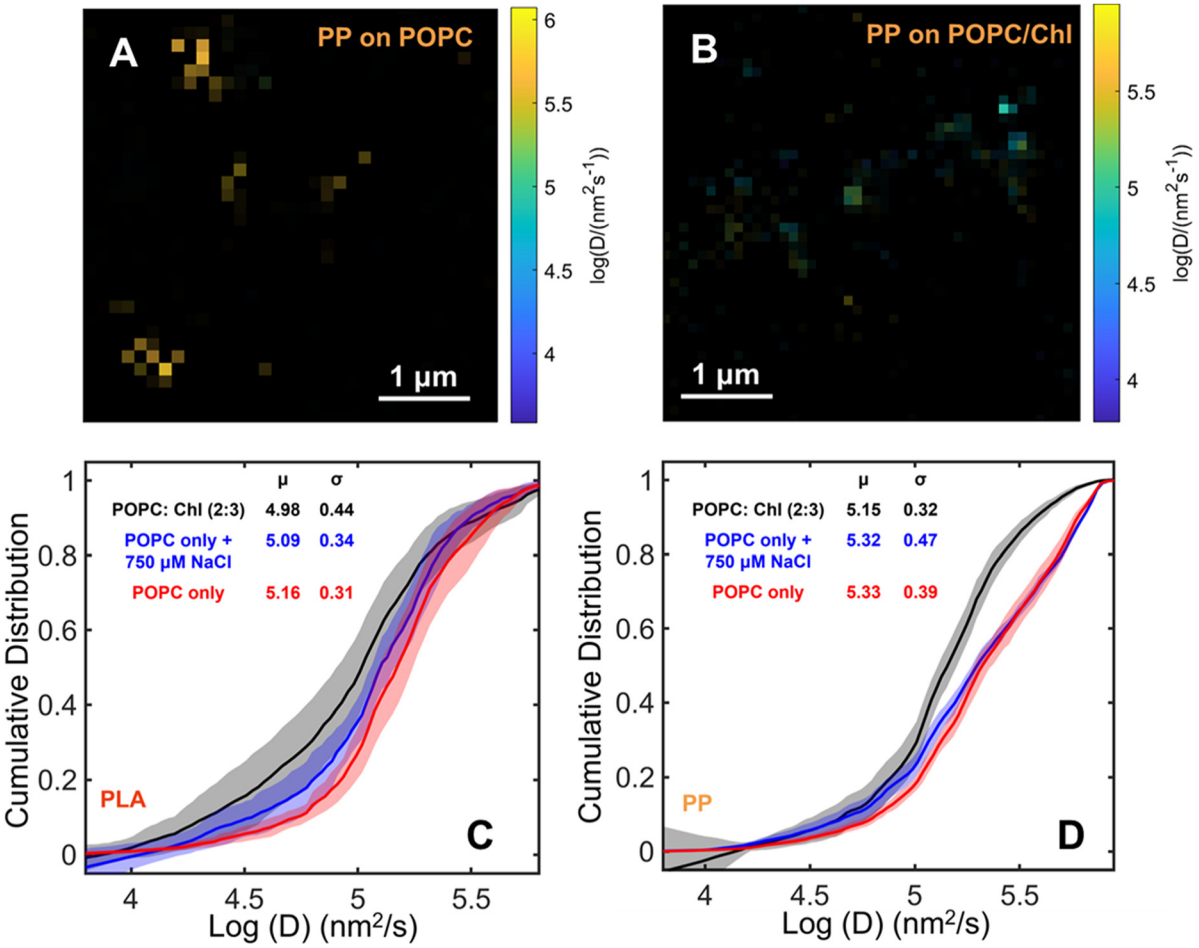

Fig. 6 Representative fcsSOFI images showing spatially resolved diffusion interaction of PP on (A) POPC and (B) POPC/Chl bilayer surface. The color bar indicates the logarithmic diffusion coefficient values in $nm^2\ s^{-1}$, with yellow regions representing higher diffusion rates and blue regions indicating slower diffusion. Differences in spatial diffusion patterns suggest that cholesterol significantly alters the membrane surface's interaction with nanoparticles, promoting heterogeneity in diffusion dynamics. Cumulative distribution of diffusion coefficients obtained from fcsSOFI analysis for (C) PLA and (D) PP interaction on POPC in buffer, POPC in salt, and 2 : 3 POPC/cholesterol bilayer surface. CDFs were calculated from 6 different ROIs in each condition, and an anomalous diffusion model fitting was performed to extract the diffusion coefficient values. The shaded regions show the standard deviation in our analysis. The mean diffusion coefficients (μ) and the slope (σ) of the CDF are shown in the inset. Slower diffusion is observed in PP and PLA surface interactions when cholesterol is on the surface.

superresolution diffusion analysis. Here we studied PP, PVC, PS, and PLA that represent significant fractions of global plastic production and are commonly found in the environment. PP (~19%), PVC (~13%), and PS (~8%) account for substantial portions of conventional plastics,[48,49] while PLA is rapidly growing as a sustainable alternative.[50] By studying these four plastics, we capture both prevalent conventional plastics and emerging bioplastics, providing a representative understanding of environmental nanoplastic behavior. Moreover, although only these four polymers were investigated here, our methods are broadly applicable and can be extended to PNPs derived from any plastic type. Our study shows the necessity of single particle measurements of engineered particles on lipid bilayer interaction and represents an essential step towards understanding environmentally relevant plastic nanoparticle effects on biomimetic systems.

Conflicts of interest

There are no conflicts to declare.

Data availability

The data supporting this article have been included as part of the supplementary information (SI). SI contains the following: schematics for our CIJ-D mixer design; absorbance and emission spectra of Nile red; calculation for determining the number density and molecules of NR dye in tagged PS-PNPs; FTIR spectra of PS, PVC, PP, PLA; hydrodynamic radius calculation; DLS autocorrelation *versus* decay time graphs and fits; particle size control by adjusting Reynold's number and dilution factor; fluorescence intensities of commercial and engineered PS-PNPs; absorbance of untagged and NR-tagged PNPs; emission spectra of NR-tagged PNPs; lateral

and confined diffusion of particles on the lipid bilayer surface; MSD *versus* time lag graph; comparison of diffusion coefficients from SPT and fcsSOFI; two videos showing localization of particles through SPT. Data will be available upon request. Supplementary information is available. See DOI: https://doi.org/10.1039/d5en00599j.

Acknowledgements

We thank the Chemistry department and Research Initiation Grant (RIG) award of Georgia State University for funding. We gratefully acknowledge the Molecular Basis of Disease (MBD) and Center for Diagnostics and Therapeutics (CDT) for graduate fellowships. The authors gratefully acknowledge the Imaging Core Facility at Georgia State University for their support and assistance in this work. We also acknowledge the machine shop facility at GSU who helped us machine the CIJ-D mixer using the Computer Numerical Control (CNC) machine (model HAAS VF 2SS).

References

1 M. MacLeod, H. P. H. Arp, M. B. Tekman and A. Jahnke, The Global Threat from Plastic Pollution, *Science*, 2021, **373**(6550), 61–65.
2 M. C. Rillig, S. W. Kim, T. Y. Kim and W. R. Waldman, The Global Plastic Toxicity Debt, *Environ. Sci. Technol.*, 2021, **55**(5), 2717–2719.
3 S. L. Wright and F. J. Kelly, Plastic and Human Health: A Micro Issue?, *Environ. Sci. Technol.*, 2017, **51**(12), 6634–6647.
4 A. Pradel, C. Catrouillet and J. Gigault, The environmental fate of nanoplastics: What we know and what we need to know about aggregation, *NanoImpact*, 2023, **29**, 100453.
5 N. Joksimovic, D. Selakovic, N. Jovicic, N. Jankovic, P. Pradeepkumar and A. Eftekhari, *et al.*, Nanoplastics as an Invisible Threat to Humans and the Environment, *J. Nanomater.*, 2022, **2022**(1), 6707819.
6 H. Shen, L. J. Tauzin, R. Baiyasi, W. Wang, N. Moringo and B. Shuang, *et al.*, Single particle tracking: from theory to biophysical applications, *Chem. Rev.*, 2017, **117**(11), 7331–7376.
7 J. S. Basuki, H. T. Duong, A. Macmillan, R. B. Erlich, L. Esser and M. C. Akerfeldt, *et al.*, Using fluorescence lifetime imaging microscopy to monitor theranostic nanoparticle uptake and intracellular doxorubicin release, *ACS Nano*, 2013, **7**(11), 10175–10189.
8 J. Caldwell, R. Lehner, S. Balog, C. Rhême, X. Gao and D. Septiadi, *et al.*, Fluorescent plastic nanoparticles to track their interaction and fate in physiological environments, *Environ. Sci.:Nano*, 2021, **8**(2), 502–513.
9 K. A. Rose, M. Molaei, M. J. Boyle, D. Lee, J. C. Crocker and R. J. Composto, Particle tracking of nanoparticles in soft matter, *J. Appl. Phys.*, 2020, **127**(19), 191101.
10 D. Fan, S. R. Bajgiran, F. S. Samghabadi, C. Dutta, E. Gillett and P. J. Rossky, *et al.*, Imaging heterogeneous 3D dynamics of individual solutes in a polyelectrolyte brush, *Langmuir*, 2023, **39**(24), 8532–8539.
11 A. Misiura, C. Dutta, W. Leung, O. J. Zepeda, T. Terlier and C. F. Landes, The competing influence of surface roughness, hydrophobicity, and electrostatics on protein dynamics on a self-assembled monolayer, *J. Chem. Phys.*, 2022, **156**(9), 094707.
12 A. Misiura, H. Shen, L. Tauzin, C. Dutta, L. D. Bishop and N. C. Carrejo, *et al.*, Single-molecule dynamics reflect IgG conformational changes associated with ion-exchange chromatography, *Anal. Chem.*, 2021, **93**(32), 11200–11207.
13 Y. Yu, M. Li and Y. Yu, Tracking single molecules in biomembranes: is seeing always believing?, *ACS Nano*, 2019, **13**(10), 10860–10868.
14 A. Pradel, H. E. Hadri, C. Desmet, J. Ponti, S. Reynaud and B. Grassl, *et al.*, Deposition of environmentally relevant nanoplastic models in sand during transport experiments, *Chemosphere*, 2020, **255**, 126912.
15 L. F. Muff, S. Balog, J. Adamcik, C. Weder and R. Lehner, Preparation of well-defined fluorescent nanoplastic particles by confined impinging jet mixing, *Environ. Sci. Technol.*, 2023, **57**(45), 17201–17211.
16 B. Nguyen and N. Tufenkji, Single-Particle Resolution Fluorescence Microscopy of Nanoplastics, *Environ. Sci. Technol.*, 2022, **56**(10), 6426–6435.
17 E. G. Karakolis, B. Nguyen, J. B. You, C. M. Rochman and D. Sinton, Fluorescent Dyes for Visualizing Microplastic Particles and Fibers in Laboratory-Based Studies, *Environ. Sci. Technol. Lett.*, 2019, **6**(6), 334–340.
18 B. Wang, S. M. Anthony, S. C. Bae and S. Granick, Anomalous yet Brownian, *Proc. Natl. Acad. Sci. U. S. A.*, 2009, **106**(36), 15160–15164.
19 D. Sil, E. Osmanbasic, S. C. Mandal, A. Acharya and C. Dutta, Variable Non-Gaussian Transport of Nanoplastic on Supported Lipid Bilayers in Saline Conditions, *J. Phys. Chem. Lett.*, 2024, **15**, 5428–5435.
20 S. Kihara, I. Köper, J. P. Mata and D. J. McGillivray, Reviewing nanoplastic toxicology: It's an interface problem, *Adv. Colloid Interface Sci.*, 2021, **288**, 102337.
21 J. Ding, Y. Huang, S. Liu, S. Zhang, H. Zou and Z. Wang, *et al.*, Toxicological Effects of Nano- and Micro-Polystyrene Plastics on Red Tilapia: Are Larger Plastic Particles More Harmless?, *J. Hazard. Mater.*, 2020, **396**, 122693.
22 C. Della Torre, E. Bergami, A. Salvati, C. Faleri, P. Cirino and K. A. Dawson, *et al.*, Accumulation and Embryotoxicity of Polystyrene Nanoparticles at Early Stage of Development of Sea Urchin Embryos Paracentrotus Lividus, *Environ. Sci. Technol.*, 2014, **48**(20), 12302–12311.
23 R. Molenaar, S. Chatterjee, B. Kamphuis, I. M. J. Segers-Nolten, M. M. A. E. Claessens and C. Blum, Nanoplastic sizes and numbers: quantification by single particle tracking, *Environ. Sci.:Nano*, 2021, **8**(3), 723–730.
24 T. Maes, R. Jessop, N. Wellner, K. Haupt and A. G. Mayes, A rapid-screening approach to detect and quantify microplastics based on fluorescent tagging with Nile Red, *Sci. Rep.*, 2017, **7**(1), 44501.
25 I. Niskanen, V. Forsberg, D. Zakrisson, S. Reza, M. Hummelgård and B. Andres, *et al.*, Determination of

nanoparticle size using Rayleigh approximation and Mie theory, *Chem. Eng. Sci.*, 2019, **201**, 222–229.

26 N. K. Khadka, R. Timsina, E. Rowe, M. O'Dell and L. Mainali, Mechanical properties of the high cholesterol-containing membrane: An AFM study, *Biochim. Biophys. Acta, Biomembr.*, 2021, **1863**(8), 183625.

27 J. Han, Z. Zhu, H. Qian, A. R. Wohl, C. J. Beaman and T. R. Hoye, *et al.*, A simple confined impingement jets mixer for flash nanoprecipitation, *J. Pharm. Sci.*, 2012, **101**(10), 4018–4023.

28 W. N. Sharratt, V. E. Lee, R. D. Priestley and J. T. Cabral, Precision polymer particles by flash nanoprecipitation and microfluidic droplet extraction, *ACS Appl. Polym. Mater.*, 2021, **3**(10), 4746–4768.

29 W. S. Saad and R. K. Prud'homme, Principles of nanoparticle formation by flash nanoprecipitation, *Nano Today*, 2016, **11**(2), 212–227.

30 B. K. Johnson and R. K. Prud'homme, Flash nanoprecipitation of organic actives and block copolymers using a confined impinging jets mixer, *Aust. J. Chem.*, 2003, **56**(10), 1021–1024.

31 A. Levin, A. Nagaev and A. Y. Sadagov, Determination of number density of particles together with measurement of their sizes by dynamic light scattering, *Meas. Tech.*, 2018, **61**, 760–766.

32 B. Shuang, J. Chen, L. Kisley and C. F. Landes, Troika of single particle tracking programing: SNR enhancement, particle identification, and mapping, *Phys. Chem. Chem. Phys.*, 2014, **16**(2), 624–634.

33 J. Schniete, A. Franssen, J. Dempster, T. J. Bushell, W. B. Amos and G. McConnell, Fast optical sectioning for widefield fluorescence mesoscopy with the mesolens based on HiLo microscopy, *Sci. Rep.*, 2018, **8**(1), 16259.

34 M. Tokunaga, N. Imamoto and K. Sakata-Sogawa, Highly Inclined Thin Illumination Enables Clear Single-Molecule Imaging in Cells, *Nat. Methods*, 2008, **5**(2), 159–161.

35 T. K. Lind, M. Cárdenas and H. P. Wacklin, Formation of supported lipid bilayers by vesicle fusion: effect of deposition temperature, *Langmuir*, 2014, **30**(25), 7259–7263.

36 M. J. Skaug, J. Mabry and D. K. Schwartz, Intermittent molecular hopping at the solid-liquid interface, *Phys. Rev. Lett.*, 2013, **110**(25), 256101.

37 L. Kisley, R. Brunetti, L. J. Tauzin, B. Shuang, X. Yi and A. W. Kirkeminde, *et al.*, Characterization of porous materials by fluorescence correlation spectroscopy super-resolution optical fluctuation imaging, *ACS Nano*, 2015, **9**(9), 9158–9166.

38 C. Dutta, L. D. Bishop, O. J. Zepeda, S. Chatterjee, C. Flatebo and C. F. Landes, Imaging switchable protein interactions with an active porous polymer support, *J. Phys. Chem. B*, 2020, **124**(22), 4412–4420.

39 F. T. Doole, T. Kumarage, R. Ashkar and M. F. Brown, Cholesterol Stiffening of Lipid Membranes, *J. Membr. Biol.*, 2022, **255**(4), 385–405.

40 M. R. Krause and S. L. Regen, The Structural Role of Cholesterol in Cell Membranes: From Condensed Bilayers to Lipid Rafts, *Acc. Chem. Res.*, 2014, **47**(12), 3512–3521.

41 F. de Meyer and B. Smit, Effect of cholesterol on the structure of a phospholipid bilayer, *Proc. Natl. Acad. Sci. U. S. A.*, 2009, **106**(10), 3654–3658.

42 J. H. Ipsen, G. Karlström, O. G. Mourtisen, H. Wennerström and M. J. Zuckermann, Phase Equilibria in the Phosphatidylcholine-Cholesterol System, *Biochim. Biophys. Acta*, 1987, **905**(1), 162–172.

43 Y. Zhang, Q. Li, M. Dong and X. Han, Effect of cholesterol on the fluidity of supported lipid bilayers, *Colloids Surf., B*, 2020, **196**, 111353.

44 R. Ashkar, M. Doktorova, F. A. Heberle, H. L. Scott, F. N. Barrera and J. Katsaras, *et al.*, Reply to Nagle *et al.*,: The universal stiffening effects of cholesterol on lipid membranes, *Proc. Natl. Acad. Sci. U. S. A.*, 2021, **118**(20), e2102845118.

45 D. Hartono, K.-L. Yang and L.-Y. L. Yung, The effect of cholesterol on protein-coated gold nanoparticle binding to liquid crystal-supported models of cell membranes, *Biomater.*, 2010, **31**(11), 3008–3015.

46 I. Sandez-Macho, M. Casas, E. V. Lage, M. I. Rial-Hermida, A. Concheiro and C. Alvarez-Lorenzo, Interaction of Poloxamine Block Copolymers with Lipid Membranes: Role of Copolymer Structure and Membrane Cholesterol Content, *Colloids Surf., B*, 2015, **133**, 270–277.

47 E. Canepa, D. Bochicchio, M. Gasbarri, D. Odino, C. Canale and R. Ferrando, *et al.*, Cholesterol hinders the passive uptake of amphiphilic nanoparticles into fluid lipid membranes, *J. Phys. Chem. Lett.*, 2021, **12**(35), 8583–8590.

48 K. Houssini, J. Li and Q. Tan, Complexities of the global plastics supply chain revealed in a trade-linked material flow analysis, *Commun. Earth Environ.*, 2025, **6**(1), 257.

49 R. Geyer, J. R. Jambeck and K. L. Law, Production, use, and fate of all plastics ever made, *Sci. Adv.*, 2017, **3**(7), e1700782.

50 L. Mou, J. Li, Y. Lu, G. Li and J. Li, Polylactic acid: A future universal biobased polymer with multifunctional performance—from monomer synthesis, and processing to applications: A review, *J. Hazard. Mater. Adv.*, 2025, 100757.